GEOPHYSICS, VOL. 71, NO. 6 (NOVEMBER-DECEMBER 2006); P. G291–G299, 11 FIGS.
10.1190/1.2348091

Adaptive finite-element modeling using unstructured grids: The 2D magnetotelluric example

Kerry Key[1] and Chester Weiss[2]

ABSTRACT

Existing numerical modeling techniques commonly used for electromagnetic (EM) exploration are bound by the limitations of approximating complex structures using a rectangular grid. A more flexible tool is the adaptive finite-element (FE) method using unstructured grids. Composed of irregular triangles, an unstructured grid can readily conform to complicated structural boundaries. To ensure numerical accuracy, adaptive refinement using an a posteriori error estimator is performed iteratively to refine the grid where solution accuracy is insufficient. Two recently developed asymptotically exact a posteriori error estimators are based on a superconvergent gradient recovery operator. The first relies solely on the normed difference between the recovered gradients and the piecewise constant FE gradients and is effective for lowering the global error in the FE solution. For many problems, an accurate solution is required only in a few discrete regions and a more efficient error estimator is possible by considering the local influence of errors from coarse elements elsewhere in the grid. The second error estimator accomplishes this by using weights determined from the solution to an appropriate dual problem to modify the first error estimator. Application of these methods for 2D magnetotelluric (MT) modeling reveals, as expected, that the dual weighted error estimator is far more efficient in achieving accurate MT responses. Refining about 15% of elements per iteration gives the fastest convergence rate. For a given refined grid, the solution error at higher frequencies varies in proportion to the skin depth, requiring refinement about every two decades of frequency. The transverse electric (TE) and transverse magnetic (TM) modes exhibit different field behavior, and refinement should consider the effects of both. An example resistivity model of seafloor bathymetry underlain by complex salt intrusions and dipping and faulted sedimentary layers illustrates the benefits of this new technique.

INTRODUCTION

Numerical modeling techniques applied to electromagnetic (EM) exploration problems — finite-element (FE) methods (e.g., Wannamaker et al., 1987; Mitsuhata and Uchida, 2004), finite-difference methods (e.g., Brewitt-Taylor and Weaver, 1976; Mackie et al., 1993), and integral equation methods (e.g., Hohmann, 1975; Wannamaker et al., 1984) — often utilize a highly structured discretization grid or volume consisting of rectangular cells or prisms that are each assigned a constant value for the modeled electrical conductivity parameter. This allows for numerically efficient solutions to the relevant EM equations; thus, structured grids are, the mainstay of state-of-the-art EM inversion routines (e.g., Newman and Alumbaugh, 2000; Zhadanov and Tartaras, 2002; Siripunvaraporn et al., 2005). However, several major drawbacks arise when attempting to approximate geologically complex models using a structured grid. Because the cell edges are usually oriented horizontally and vertically, sloping and highly variable structures are usually approximated using a series of discrete jumps or stair steps in the model parameter values. Although these can be made sufficiently small to ensure accuracy, the resulting grid may have cells with very large aspect ratios (for instance 100:1), which are well known to seriously degrade the convergence of the Krylov solvers commonly used for the numerical linear system. Additionally, fine discretization in the model center extends both vertically and horizontally to the grid edges, greatly increasing the number of model cells and hence increasing the computer memory and run-time requirements.

Several solutions for handling more complexity have been pro-

Manuscript received by the Editor September 14, 2005; revised manuscript received March 11, 2006; published online October 6, 2006; corrected version published online October 12, 2006.
[1]University of California San Diego, Scripps Institution of Oceanography, 9500 Gilman Drive, La Jolla, California 92093-0225. E-mail: kkey@ucsd.edu.
[2]Sandia National Laboratories, Geophysics Department, P. O. Box 5800 MS-0750, Albuquerque, New Mexico 87185. E-mail: cjweiss@sandia.gov.

posed and include structured triangular FEs (Wannamaker et al., 1987) and conductivity averaging (Aprea et al., 1997; Baba and Seama, 2002). Yet these methods have underlying rectangular grids and in practice can present a cumbersome grid design challenge for modeling highly variable structures. Of particular importance are land and seafloor variations, which can greatly affect EM responses because the measurement locations are usually situated there (e.g., Baba and Seama, 2002; Schwalenberg and Edwards, 2004).

We overcome the structured grid limitations by implementing an adaptive FE method that uses unstructured elements. The term unstructured means that the elements are only constrained to be shape regular (triangles) and that element edge lengths can vary from side to side and element to element. An unstructured grid can easily be designed to conform exactly to straight-edged boundaries of any slope. Arcuate boundaries can be approximated to the required precision using many small elements. Thus, unstructured grids are highly suitable for modeling arbitrarily shaped interfaces. Because unstructured elements can rapidly grow larger with distance, small discretization in the model center does not have to extend to the model edges and thus memory requirements can be kept relatively low. A constraint on the minimum inner angle of the triangular elements can be used to ensure that no elements are slivers (the triangular element equivalent of large aspect ratio rectangular cells), which can cripple the efficiency of the Krylov solver.

Fast and robust triangulation routines for generating quality unstructured 2D grids are readily available (e.g., Shewchuk, 1996, 2002). However, for arbitrarily complex models, it is difficult to construct an optimal FE grid that balances numerical efficiency (requiring fewer elements) with numerical accuracy (requiring more elements). A well-accepted solution to this dilemma is the adaptive FE method, in which the solution is calculated iteratively using successively refined grids until converging to the desired tolerance. The decision of which elements to refine can be accomplished using an a posteriori error estimation scheme (e.g., Ainsworth and Oden, 2000) that estimates the normed error in the solution, or its gradient, over each element.

In this work, we apply the unstructured FE method and an adaptive refinement technique to the 2D magnetotelluric (MT) problem. For reviews of the MT method, see Vozoff (1991) and Simpson and Bahr (2005). While the engineering and other communities have embraced adaptive unstructured grids for quite some time now, this appears to be the first application to EM geophysics in general. Since the MT practitioner is generally interested in the solution quality only at the measurement locations (a series of sites along the air-land or sea-seafloor boundaries), simple adaptive refinement is not the most efficient way to reach an acceptable solution. Instead, we use a goal-oriented adaptive refinement algorithm in which the estimated error for each element is weighted by its influence to the solution at the MT sites. Thus, refinement only occurs where the solution is inaccurate and where that inaccuracy corrupts the solution at the (possibly distant) MT sites. The basic error estimator is calculated using a superconvergent gradient recovery operator (Bank and Xu, 2003), and the appropriate weights are determined by the solution of a dual/adjoint problem (Ovall, 2004, 2006). We note that this adaptive method is very general and could also be applied to many other geophysical problems.

In the following sections, we review the secondary field formulation for 2D MT and present the corresponding FE solution. We then describe the a posteriori error estimation scheme and the dual method used to weight the error estimates. We verify the method's accuracy and study its convergence properties by comparison with an analytic 2D MT code. Finally, we provide an example of using the adaptive method to model the MT response of a complex resistivity structure that is realistic for the offshore exploration environment.

PROBLEM STATEMENT

For the case where the electrical conductivity σ is variable in only two coordinates (y,z), the two independent modes of MT excitation (TE: transverse electric; TM: transverse magnetic) give rise to an uncoupled set of partial differential equations in terms of the strike-aligned electric E_x and magnetic H_x fields:

$$\text{TE:}\ -\nabla\cdot\nabla E_x + i\omega\mu_0\sigma E_x = -i\omega\mu_0 J_0 \tag{1}$$

and

$$\text{TM:}\ -\nabla\cdot\frac{1}{\sigma}\nabla H_x + i\omega\mu_0 H_x = -i\omega\mu_0 M_0, \tag{2}$$

where ω is the angular frequency, a uniform magnetic permeability $\mu_0 = 4\pi\times 10^{-7}$ H/m is assumed, and the TE and TM modes are driven by laterally uniform electric $J_0(z)$ and magnetic $M_0(z)$ sources located above the earth's surface.

One approach to solving equations 1 and 2 is to split the electric and magnetic fields into primary and secondary components, corresponding to the fields (E_x^0, H_x^0) arising from some reference conductivity model σ_0 and the fields (E_x', H_x') arising from the conductivity difference $\sigma - \sigma_0$ with the model of interest (e.g., Coggon, 1971). The total fields are found by summing their respective constituents:

$$E_x = E_x^0 + E_x' \quad \text{and} \quad H_x = H_x^0 + H_x'. \tag{3}$$

The reference model σ_0 is typically formulated so that it admits some easily obtained and well-behaved solution [e.g., the 1D layered earth $\sigma(z)$ where TE and TM modes are equivalent and the analytic solution is simple to derive]. The primary advantage to this approach lies in the fact that the FE grid only needs to accurately capture the secondary field variations, which tend to be more localized than total field variations; thus, a grid with fewer elements can often be used.

The secondary electric and magnetic fields also satisfy an uncoupled pair of partial differential equations for the TE mode,

$$-\nabla\cdot\nabla E_x' + i\omega\mu_0\sigma E_x' = -i\omega\mu_0(\sigma-\sigma_0)E_x^0, \tag{4}$$

and the TM mode,

$$-\nabla\cdot\frac{1}{\sigma}\nabla H_x' + i\omega\mu_0 H_x' = \hat{x}\cdot\nabla\times\left(1-\frac{\sigma_0}{\sigma}\right)\mathbf{E}^0. \tag{5}$$

Note that $\mathbf{E}^0$ in the right-hand side of equation 5 is the 1D electric field obtained for a TM source term and is equivalent to E_y^0. For both equations, the right-hand side can be described as a source term arising from the interaction of the conductivity perturbation $\sigma - \sigma_0$ and the primary electric field $\mathbf{E}^0$.

Consider a triangulation of the model domain Ω composed of M Delaunay triangles (elements) described by N vertices and the N-dimensional vector spaces V and V_0. Equation 4 for the TE mode can be reexpressed as the variational problem to find $u\in V$ such that

$$B(v,u) = f(v) \text{ for all } v\in V_0, \tag{6}$$

where

$$B(v,u) = \int_\Omega k\,\nabla v \cdot \nabla u\, d\Omega + \int_\Omega quv\, d\Omega \qquad (7)$$

and

$$f(v) = \int_\Omega vs\, d\Omega, \qquad (8)$$

where $u = E'_x, k = 1, q = i\omega\mu_0\sigma, s = -i\omega\mu_0(\sigma - \sigma_0)E^0_x$ and where a homogeneous boundary condition has been applied. For the TM mode, the continuity of electric current normal to boundaries is required; after a bit of tedious manipulation, equation 5 can be reexpressed as the variational problem to find $u \in V$ such that

$$B(v,u) = g(v) \text{ for all } v \in V_0, \qquad (9)$$

where $B(v,u)$ retains its definition given in equation 7 but with $u = H'_x, k = 1/\sigma$ and $q = i\omega\mu_0$. The right-hand side is given by

$$g(v) = \int_\Omega \frac{\partial v}{\partial z}\left(1 - \frac{\sigma_0}{\sigma}\right)E^0_y d\Omega. \qquad (10)$$

Equations 6 and 9 can be solved in the usual way using FEs, resulting in the solution vector u_h. Here we use unstructured triangular elements with linear basis functions. For a general review of FE methods, see Lapidus and Pinder (1999). Note that in contrast to a previous development of the FE method for the TM mode problem (e.g., Wannamaker et al., 1987), our solution possesses no boundary integrals in its formulation. The formulation given here fully embraces abrupt changes in electrical conductivity through rigorous treatment of the boundary integrals as they arose in the manipulations leading to the variational problem. No such assumptions as smooth conductivity or spatially averaged conductivity are needed here. Rather, the charge buildup effects on these interfaces are captured in their entirety by the volume-integral sourcing function in equation 10.

After numerically solving equations 6 and 9 for E'_x and H'_x, the remaining field components can be found through Faraday's and Ampere's laws, shown as

$$\frac{\partial E'_x}{\partial z} = -i\omega\mu H'_y, \qquad (11)$$

$$\frac{\partial E'_x}{\partial y} = i\omega\mu H'_z, \qquad (12)$$

$$\frac{\partial H'_x}{\partial z} = \sigma E'_y + (\sigma - \sigma_0)E^0_y, \qquad (13)$$

$$\frac{\partial H'_x}{\partial y} = -\sigma E'_z. \qquad (14)$$

The primary and secondary fields are added together to form the total fields, which are then used to compute the various MT transfer functions. For instance, the MT impedances for the TE and TM modes are

$$Z_{xy} = Z_{\text{TE}} = \frac{E_x}{H_y}, \quad Z_{yx} = Z_{\text{TM}} = \frac{E_y}{H_x}.$$

The commonly used MT apparent resistivity transformation ρ_{xy} and impedance phase ϕ_{xy} are defined as

$$\rho_{xy} = \frac{1}{\omega\mu}|Z_{xy}|^2, \qquad (15)$$

$$\phi_{xy} = \arctan(Z_{xy}), \qquad (16)$$

and similarly for the yx-components.

A POSTERIORI ERROR ESTIMATION

Methods for a posteriori error estimation have been studied extensively for the past two decades, and a review of the major accomplishments up to the end of the 1990s is presented in Ainsworth and Oden (2000). A recent class of techniques called recovery-based error estimators utilize a postprocessed, or recovered, gradient approximation. The general idea is that the piecewise constant FE solution gradient ∇u_h implicit in the use of linear basis functions for each element can be greatly improved in accuracy through a variety of averaging or projection techniques to form a recovered gradient $\mathcal{R}\nabla u_h$. A local error estimator η_e for each element is then formed by integrating the difference between the recovered and piecewise constant gradients, stated as

$$\eta_e \equiv \|\mathcal{R}\nabla u_h - \nabla u_h\|_{L_2(e)}, \qquad (17)$$

where the L_{2_z} norm is invoked. The effectiveness of recovery techniques for a posteriori error estimation is because of the superconvergence property (e.g., Ovall, 2004, chapter 3) of many recovery operators, which leads to asymptotically exact error estimators, stated as

$$\frac{\|(\mathcal{R} - I)\nabla u_h\|_{L_2(\Omega)}}{\|\nabla(u - u_h)\|_{L_2(\Omega)}} \to 1 \text{ as } h \to 0, \qquad (18)$$

where u is the true solution to the differential equation, I is an identity operator, and h is the diameter of the circumscribing circle for each element. For general unstructured grids, a recovery operator with the superconvergence property is proved in Bank and Xu (2003). They define the recovery operator as,

$$\mathcal{R}\nabla u_h = S^m Q_h \nabla u_h, \qquad (19)$$

where Q_h is the global L_2 projection operator, stated in bilinear form as

$$(Q_h\nabla u_h, v) = (\nabla u_h, v), \qquad (20)$$

and S^m is a smoothing operator using m smoothing iterations. In other words, $Q_h\nabla u_h$ is the L_2 projection of the piecewise constant element gradient ∇u_h onto the nodal basis, which is then smoothed using S^m. For the smoothing operations, the partial solution to

$$\nabla^2(Q_h\nabla u_h) = 0 \qquad (21)$$

is computed using m conjugate gradient iterations. This method, referred to here as the basic error estimator (BEE), could easily be adapted to many numerical problems since its form is independent of the problem being solved. The recovery operator $\mathcal{R}$ also proves useful for MT because the fidelity of the desired MT responses depends on both the strike parallel field and its gradients. For the TM mode, some care needs to be taken during the L_2 projection and gradient

smoothing because discontinuous gradients in the secondary magnetic field need to be permitted at conductivity boundaries. Hence, for the TM mode we solve equations 20 and 21 locally over regions of constant conductivity.

ERROR WEIGHTING USING THE DUAL SOLUTION

The electric and magnetic fields (and their spatial gradients) need to be known precisely only at the MT measurement sites, usually discrete points on the air-land or sea-seafloor boundary. However, refinement based on the error estimator in equation 17 concentrates on elements with the largest errors, which can often lead to several refinement steps that have little effect on the MT responses, resulting in an unnecessarily large computation burden. Simply increasing the refinement in the proximity of the MT sites would not necessarily work, as it is well known for elliptic equations that errors in nonlocal portions of the FE grid can corrupt the local solution — an effect appropriately termed pollution.

A well-accepted strategy for handling pollution is through the use of the dual or adjoint problem, which provides a way to quantify the local influence of nonlocal errors. A recent study that uses the same framework as Bank and Xu (2003) applies the dual method for obtaining functional error estimates, which are then used as a refinement criterion for adaptive FE modeling (Ovall, 2004, 2006). Below, we review this approach and suggest how it should be applied to the 2D MT problem.

The dual operator B^* is defined relative to the primal operator B (defined for equations 6 and 9) as $B^*(w,v) \equiv B(v,w)$. The dual problem is to find w that satisfies

$$B^*(w,v) = G(v) \text{ for all } v \in V_0, \tag{22}$$

where G is a given functional, in this case assumed to be some functional of the solution error $(u - u_h)$. We then have

$$\begin{aligned} G(u - u_h) &= B^*(w, u - u_h) = B(u - u_h, w) \\ &= B(u - u_h, w - w_h), \end{aligned} \tag{23}$$

where w_h is the FE solution for w and we invoke Galerkin orthogonality to achieve the last term on the right-hand side. Using the definition of B from the MT problem statement, the right-hand side can be written as

$$\begin{aligned} B(u - u_h, w - w_h) = \int_\Omega & k\nabla(u - u_h) \cdot \nabla(w - w_h) \\ & + q(u - u_h)(w - w_h) d\Omega. \end{aligned} \tag{24}$$

For general earth conductivities and the low frequencies used in MT, $k \gg q$, suggesting that the left side of the integral will be dominant. The two gradient terms can be approximated using the superconvergent gradient recovery operator. Thus,

$$B(u - u_h, w - w_h) \approx \int_\Omega k(\mathcal{R} - I)\nabla u_h \cdot (\mathcal{R} - I)\nabla w_h \, d\Omega. \tag{25}$$

Equation 25 is an approximation of the global error functional G, which can be computed using u_h and w_h, the solutions to the primal and dual problems, respectively. For the local error estimate for each element, Ovall (2004) suggests using an approximation that is numerically easier to evaluate, referred to as dual error estimate weighting (DEW):

$$\hat{\eta}_e \equiv \left\| (\mathcal{R} - I)\nabla u_h \right\|_{L_2(e)} \left\| k(\mathcal{R} - I)\nabla w_h \right\|_{L_2(e)}. \tag{26}$$

Simply put, $\hat{\eta}_e$ is just a weighted version of the basic error estimator η_e (equation 17) where the weights are determined from the solution of the dual problem. To compute w_h using equation 22, we need to define the error functional G. Several suggestions are offered in Ovall (2004, 2006); we use the functional that approximates the H^1 seminorm of the error in the subdomain Ω_s:

$$G(v) \equiv \int_{\Omega_s} (\mathcal{R} - I)\nabla u_h \cdot \nabla v \, d\Omega_s, \tag{27}$$

where Ω_s is the possibly discontinuous subdomain of elements that contain MT sites. In elements outside Ω_s, the value of G is defined to be zero.

In summary, the global solution w_h to the dual problem (equation 22) is calculated using the functional error G (equation 27) as a sourcing function. The recovered gradients $\mathcal{R}\nabla u_h$ and $\mathcal{R}\nabla w_h$ are then used in equation 26 to form the weighted error estimator $\hat{\eta}$ for each element.

IMPLEMENTATION DETAILS

We have implemented the adaptive refinement scheme into a FORTRAN-90 program named MARE2DMT. The background conductivity σ_0 can be defined as a 1D layered model using the conductivity values of elements located along either the left side or right side of the FE grid or can be a user-defined layered model. Regardless of the background model, the outer boundary conditions are set so that the total fields (i.e., primary plus secondary) along the left and right FE grid boundaries will be equal to the 1D fields produced by the layered conductivity profiles along each respective boundary. For vertices lying along the top and bottom boundaries, the secondary field is set to a cosine taper interpolation of the left and right side boundary values. For highly 2D models, we recommend using a background model that has a single layer which spans the depth range of complex structures such as bathymetry, salt domes, and other strong 2D features. This is because the term $\sigma - \sigma_0$ in the source integral can become ambiguous when an element straddles a background model layer. Although conductivity averaging could be used in this instance, we find it is more accurate to use a single background model layer over these depths, with other possible layers above and below this layer. For instance, a background model for a marine MT study could contain three layers: air, seawater, and mantle. The seawater layer would span from the sea surface down to well below the seafloor and any crustal structure.

The linear FE systems that arise from the TE and TM modes (equations 6 and 9) can each be stated as

$$\mathbf{Lu} = \mathbf{s}, \tag{28}$$

where $\mathbf{L}$ is an $N \times N$ sparse matrix arising from the exact evaluation of the basis function integrals, $\mathbf{u}$ is the N vector of unknown nodal field values, and $\mathbf{s}$ is the N vector of source function integrals. The sparsity of $\mathbf{L}$ makes it inefficient and expensive to store and invert when solving for $\mathbf{u}$. Instead, we use a matrix-free iterative solver approach based on the quasi-minimal residual (QMR) method (Freund and Nachtigal, 1994). In the QMR method, the solution to

equation 28 is found iteratively by rching through expanding Krylov subspaces of the linear system. This approach is matrix free in that Krylov methods only require computing the action of the matrix on an arbitrary vector but not explicit storage of the matrix itself. Thus, for an arbitrary solution vector $\mathbf{u}$, we compute the vector $\mathbf{Lu}$ additively by summing up the contribution $\mathbf{L}_e\mathbf{u}_e$ from each element. For N degrees of freedom in the linear system, the storage requirements of QMR are only $10N$. We use simple Jacobi scaling as a preconditioner to speed up the rate of convergence for QMR, but other more complicated preconditioners could also be used. The linear system arising from the dual problem (equation 22) is also solved using QMR. The L_2 projection (equation 20) results in a well-conditioned mass matrix that is easily inverted using only a few QMR iterations. For the smoothing operations S^m, the left-hand side of equation 21 results in a stiffness matrix and is partially solved using m preconditioned conjugate gradient (PCCG) iterations.

After solving the primal and dual problems, the error estimator $\hat{\eta}$ (equation 26) is calculated for each element. The r percent of elements with the largest $\hat{\eta}$ values are selected for refinement. After a refined grid is generated, a new FE solution and error estimator $\hat{\eta}$ are computed, and the process is repeated iteratively until the solution converges to the desired tolerance. To speed up the solution time on subsequently refined grids, the QMR solver can be started using the linear interpolation of the previous solution onto the current grid.

Element refinement is done using external calls to Triangle (Shewchuk, 1996, 2002), an open-source constrained and conforming Delaunay triangulation code. Triangle can rapidly generate a high-quality triangulation that conforms to an input set of vertices and connecting line segments; it has no practical limit on the amount of complex structure included in the grid. The triangulation quality is measured by the minimum edge angle α permissible in any triangular element. Small angles in FEs are known to form an ill-conditioned stiffness matrix that can seriously degrade the convergence of Krylov solvers. Triangle also has difficulty generating a triangulation when $\alpha > 33°$, and we have found through experience that $20° < \alpha < 32°$ works well. Grid refinement is accomplished by an optional input file to Triangle that specifies maximum area constraints for refining elements in an existing mesh. In our example, we specify that the r percent of elements with largest $\hat{\eta}$ values have maximum area constraints of one-half their current size. The number of elements in the grid then increases by at least $2r$ percent upon each refinement step, although the exact number can be much greater than this because Triangle refines existing grids by adding new vertices and then recomputing an optimal triangulation of those vertices. Refinement using Triangle usually takes an insignificant amount of time when compared to solving the FE system.

The recovered gradient $\mathcal{R}\nabla u_h$ is used to compute the strike normal components of the MT fields using equations 11–14. For sites located along structural boundaries (the air-land interface or the sea-seabed interface), we use the recovered gradients from the more conductive side of the boundary because they are usually more well behaved. We also note that for the TM mode, air elements are not required because vertical electric currents are not permitted at the air-land boundary.

COMPARISON WITH ANALYTIC CALCULATION

We verify the new algorithm by comparing its results with an analytic solution for a simple segmented slab model (Weaver et al., 1985, 1986). The model is illustrated in Figure 1 and consists of a 100-km–thick slab divided into a 5-km wide, 1-ohm-m region, bound on the left and right by 10- and 50-ohm-m and 50 ohm-m regions. The analytic solution has a perfect conductor underneath the slab, which we approximate in the FE grid by setting resistivity to 10^{-8} ohm-m. MT responses at the 100-s period were computed for 197 sites atop the slab at lateral positions between –100 and 100 km. The adaptive FE algorithm was run until either an acceptable MT response misfit was obtained or the number of vertices grew excessively large. Both the BEE and DEW techniques were tested. Figures 2 and 3 show the agreement of the MT fields computed using the analytic calculation and the FE method (using the final grid obtained using DEW refinement). Because the TM mode H_x field at the air-land interface is constant, only the E_y field is shown. Figure 4 illustrates the convergence rate for both BEE and DEW refinement. As expected, DEW refinement far outperforms BEE refinement. For the TE mode, DEW achieves a 1% root mean square (rms) misfit level using about 5000 vertices, while extrapolation for BEE suggests about 10 more refinement iterations and about 20 times more vertices are needed to achieve the same misfit. For the TM mode, DEW achieves a 1% rms misfit level using about 10,000 vertices, while BEE never reaches an acceptable misfit and instead converges to a constant 20% misfit for the last 10 iterations.

Figure 5 shows the coarse starting grid and the BEE and DEW grids for the TE mode after 18 refinement steps. The vertical 1D conductivity profile of the left segment was used for the background model σ_0, so both the middle and right segments had nonzero $\sigma - \sigma_0$ and hence had nonzero secondary field source terms. The TE

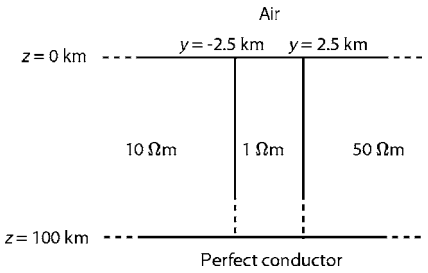

Figure 1. Model used for comparison of adaptive FE and analytic calculations.

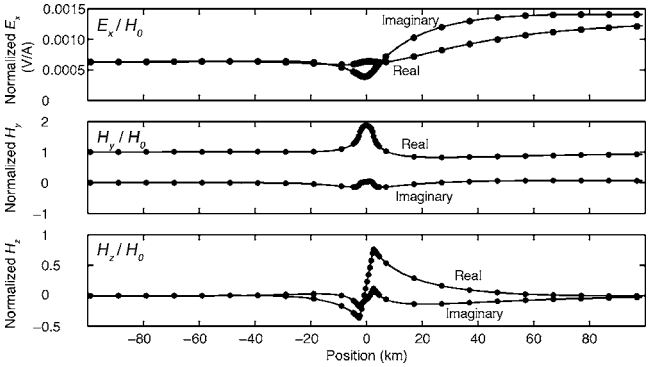

Figure 2. Comparison of the real and imaginary TE fields at 100 s period from the analytic and FE calculations after 18 DEW iterations. The FE solution is plotted as lines and every second point of the analytic solution is plotted as black dots. Field values are normalized by the magnetic field H_0 at $x = -100$ km.

mode BEE refinement is concentrated almost uniformly throughout both the middle and right segments, whereas the DEW refinement is centered around the MT site locations, with a small bias towards the middle and right segments over the left segment. Figure 6 shows the twentieth refinement grids generated for the TM mode. It is clear why the BEE refinement resulted in a constant 20% misfit — most of the refinement is concentrated near depths of 100 km in both the middle and right segments. In this region, the secondary field source currents are nonzero and the solution contains a sharp gradient as it attenuates to zero in the basal conducting layer. This region is far enough away from the MT sites that the massive amount of refinement has little effect on the MT responses. This is sharply contrasted by the effectiveness of the DEW refinement, where new elements were created near the MT sites and in the middle segment and only a small amount of refinement occurred on the right segment near the 100-km depth boundary.

For both modes and refinement techniques, the maximum misfit over all data is about 2–10 times larger than the rms misfit. For the TM mode, the maximum misfit sometimes increases by up to a factor of two on subsequent interactions. This is as expected, given the way Triangle refines existing grids by using a hierarchy of vertices but not a hierarchy of elements. Sometimes old elements are replaced by new elements that have slightly worse recovered gradients, the case usually being that an element is inverted from its original position. However, subsequent grid refinement effectively refined these elements and the algorithm converged to an acceptable solution. This effect is not seen in the TE mode because the secondary field E_x' exhibits more smoothly varying spatial gradients.

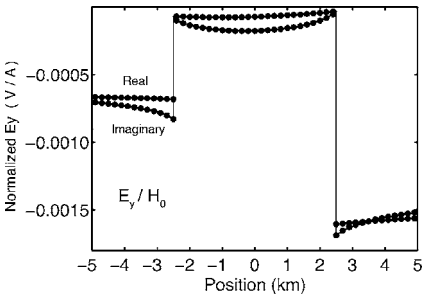

Figure 3. Comparison of the real and imaginary components of the TM mode E_y field at 100 s period from the analytic and FE calculations after 20 DEW iterations. Only the solution at $-5 \le x \le 5$ km is shown. The FE solution is plotted as lines and every fifth point of the analytic solution is plotted as black dots. Field values are normalized by the magnetic field H_0 at x = −100 km.

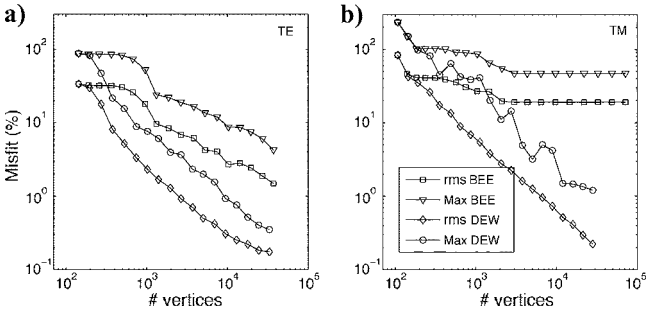

Figure 4. Convergence of the MT responses for grid refinement using the BEE and DEW, shown as the rms misfit and maximum misfit for the (a) TE and (b) TM responses at 100 s.

An efficiency test for various amounts of grid refinement per iteration is shown in Figure 7. The results indicate that about 15% refinement gives the fastest decrease in misfit, which was used for the plots in Figure 4. However, our experience suggests that this number will vary slightly, depending on the model complexity and on the choice of the background model σ_0. Another test was done to find the optimal number of smoothing iterations m to use for equation 21, which Bank and Xu (2003) show is two when considering the error in the entire model domain. Although not shown here, our tests for the TE mode indicate that the recommended two smoothing iterations can actually slightly degrade the gradient estimates at MT sites, resulting in up to twice as many vertices required to achieve the same rms gradient accuracy as zero smoothing iterations. This is in part because the MT sites are located along a conductivity interface where the

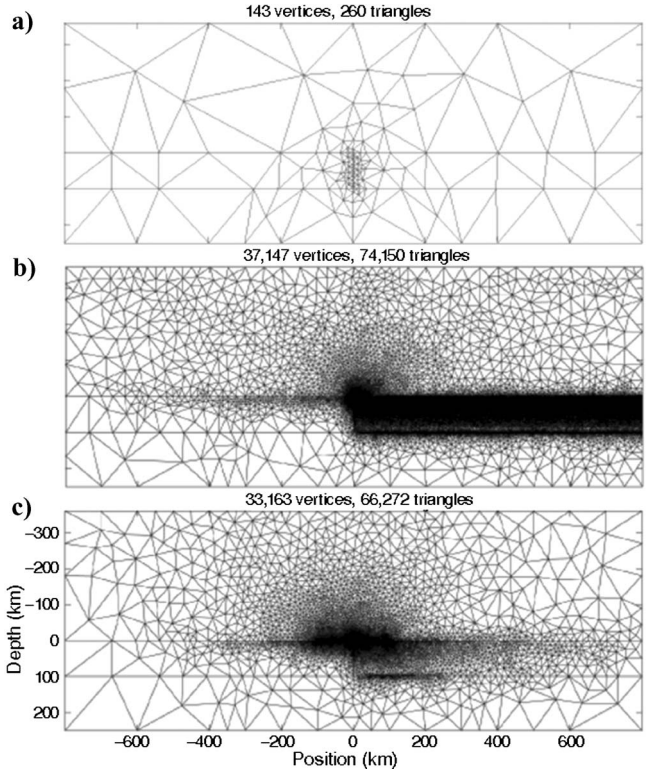

Figure 5. FE grid comparison for the TE mode calculation at 100 s. (a) Coarse starting grid, (b) eighteenth refined grid using BEE and (c) DEW based refinement. MT sites were located between 100 and 100 km.

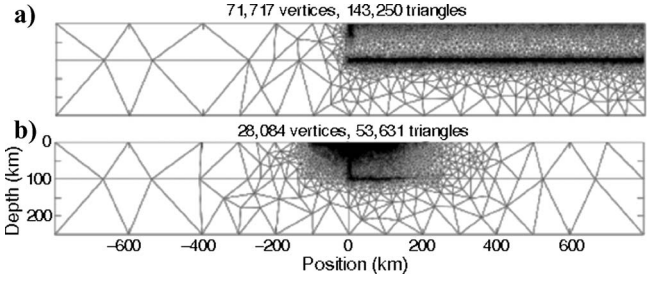

Figure 6. FE grid comparison for the TM mode calculation at 100 s. (a) Twentieth refined grid using BEE and (b) DEW-based refinement.

gradient has an abrupt change in slope, which is being smeared out by the smoothing iterations.

For our final test, we analyzed the frequency dependence of the TE grid. Using the 100-s period optimized grid, we computed FE solutions at periods from 1 to 10,00 s. The misfits for the E_x and H_y components are shown in Figure 8. At shorter and longer periods, the misfit is larger than at 100 s. At the longest periods, the misfit begins to decrease as the skin depth of the EM fields increases and the EM fields become less sensitive to the relatively shallow 2D slab and more sensitive to the basal conducting half-space. At periods shorter than 100 s, the E_x maximum misfit behaves as $T^{-0.56}$, where T is the period in seconds, and the rms misfit behaves as $T^{-0.23}$. The maximum misfit for short periods appears to be inversely related to the EM skin depth, which is proportional to $T^{0.5}$. Given this scaling, a grid converged to about 0.1% accuracy could be used to give a 1% accurate response at a period 100 times shorter. Similar arguments probably hold for the long period limit, depending on the model structure. A safe strategy for computing a broadband MT response would be to use refinement for every two decades of period, thus ensuring accurate solutions for the decade of periods on both sides of the refinement periods.

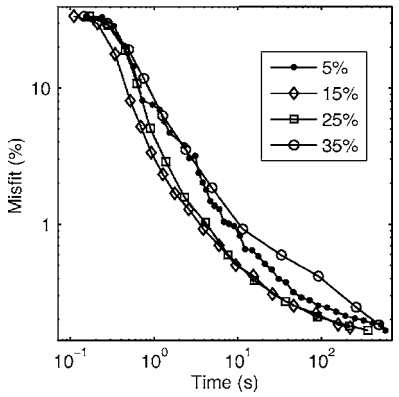

Figure 7. Efficiency of grid refinement for various amounts of DEW refinement per iteration.

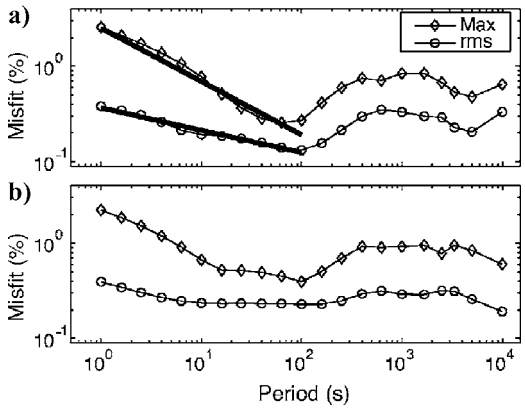

Figure 8. TE mode misfit as a function of period when using the 100 s optimized grid at other periods. Maximum misfit and rms are shown for (a) E_x and (b) H_y. The slopes of thick lines are proportional to $T^{-0.56}$ and $T^{-0.23}$, where T is the period in seconds.

COMPLEX SEAFLOOR MODEL

Here we present an example that highlights the unique capabilities of adaptive refinement. Our goal is to obtain accurate MT responses at 1–10,000-s periods for a model that bears resemblance to structures found along the Sigsbee Escarpment, offshore in the northern Gulf of Mexico (e.g., Orange et al., 2004). Figure 9 shows the central portion of the model. The blue resistive features above 7 km depth are hypothetical salt domes and intrusions, the red-orange layering corresponds to a sedimentary sequence, and small yellow resistive features are near-surface gas hydrate accumulations. The entire domain extends from –100 to 200 km in depth and from –500 to 500 km in width. Below 25 km depth, the model contains a horizontal layer of 1 ohm-m, which attenuates the long-period secondary fields by several skin depths before they diffuse to the model boundaries. A coarse initial grid that exactly conforms to this model was generated in Triangle in just a fraction of a second and contains 1789 vertices and 3526 elements. Thirty MT sites were positioned along the seafloor at lateral positions of 0–42 km. The background 1D model for σ_0 was chosen to contain four layers: air, conductive seawater, resistive basement, and the terminating conductor. To avoid the degenerate case of elements that span across a background model layer boundary, the seawater background model was extended to a depth of 8 km, well beneath any of the 2D structures.

Adaptive refinement iterations were done for periods of 10 and 1000 s. For each iteration, the error estimator $\hat{\eta}$ was computed for both the TE and TM modes and at both refinement periods, and 15% of elements with the highest values were refined in Triangle. Since the DEW scheme results in a steady monotonic convergence of the rms misfit, we used a simple convergence test of differencing the MT responses from consecutive iterations. After nine iterations, the differences had an rms value of about 0.1% and a maximum value of 0.8%, so the refinement iterations were stopped. The final grid uses 20,643 vertices and 41,231 elements.

The central portion of the grid and the total normed error for the eighth refinement are shown in Figure 10. The grid refinement is concentrated in two general regions: around the MT sites and along the boundaries of the resistive salt bodies. In the vicinity of the MT sites, the smallest elements are about 30 m diameter, or about one-tenth the skin depth in seawater at the 1 s period. The small elements on the resistive salt boundaries occurs on the interior edge of the salt. Although not shown here, we also tried using BEE refinement, which results in the exact opposite effect, with the refinement occurring on the exterior of the salt. This counterintuitive finding actually has a logical explanation. For the TM mode, BEE determines that large gradient errors in the H_x' field are present on the exterior of the salt, corresponding to boundary charge effects; therefore, finer ele-

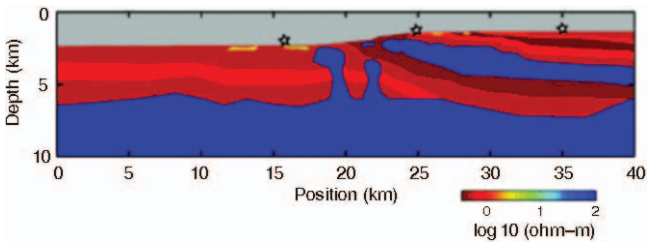

Figure 9. Central portion of the complex seafloor model. Colors correspond to resistivity values. Gray indicates seawater resistivity. Stars show the locations of the three MT responses plotted in Figure 11.

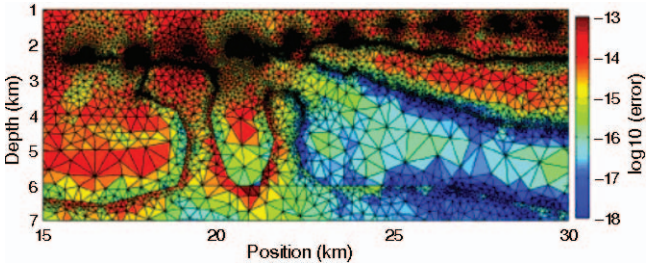

Figure 10. Error estimator $\hat{\eta}$ for the eighth refinement iteration grid. Colors show the $\log_{10}$ value of the normed error estimator, summed for both TE and TM modes at 10- and 1000-s periods. Only the central portion of the grid is shown.

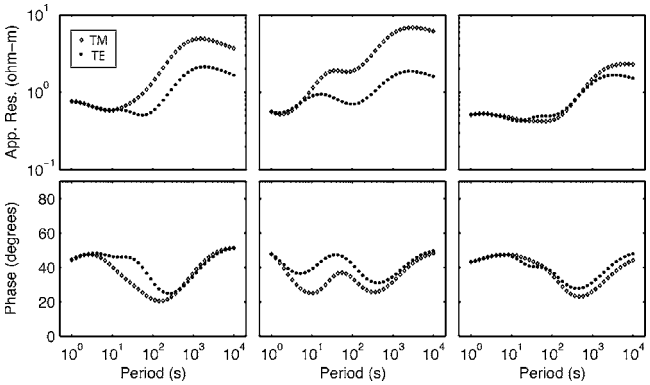

Figure 11. MT apparent resistivity and phase responses for the three sites shown in Figure 9.

ments are required there. However, for DEW, the dual solution weights effectively reverse the situation. This occurs because the MT fields have larger skin depths inside the salt, so anomalous fields generated on the salt boundary are able to effectively diffuse through the salt and up to the MT sites. Likewise, errors in the solution can effectively pollute the MT sites through diffusion through the resistive elements. Therefore, an accurate solution on the resistive side of the boundary is more important in this instance.

In Figure 11 we show broadband MT responses from three seafloor sites, which were computed using the strike parallel and perpendicular fields. The responses are clean looking and contain the complex signature of underground resistivity features.

CONCLUSIONS

The unstructured and adaptive FE algorithm for MT modeling provides a unique tool for studying the response of complex 2D structures. Based on the tests shown, we can recommend the following conclusions for implementing this technique: The adaptive algorithm can be started from a coarse grid that conforms to any imposed structural boundaries. Refinement iterations should be performed for at least one period every two decades and should be done for both TE and TM modes. DEW should be used to guide the refinement. In addition, about 15% refinement per iteration yields the fastest convergence rate. Gradient smoothing operations are unnecessary for surface MT sites. Finally, a simple and effective convergence test is to difference the results from consecutive iterations.

The converged grids show some interesting properties that reflect the sensitivity of MT. The DEW-based refinement yields grids with the smallest elements near the MT sites. These elements have diameters of about one-tenth a skin depth at the shortest period when the grid has converged to about 0.1%–1% misfit. Additional regions of heavy grid refinement are observed along select resistivity boundaries that would otherwise pollute the responses at the MT sites. A counterintuitive finding for the complex seafloor model reveals that refinement along the interior edge of the resistive salt is more important for the MT response accuracy than refinement in the conductive regions exterior to the salt.

Adaptive refinement is particularly well suited to handle marine MT profiles across regions of large and predominantly 2D topographic variations such as spreading ridges, the continental slope, and faulted margins. The method could be applied to other EM techniques, such as the many forms of controlled-source EM sounding. Variations of the adaptive method may prove effective for improving the stability of inversions. As the inversion model parameters are updated, regridding and refinement could ensure the accuracy of the forward solution and Frechet derivatives. Sharp boundary inversions could be equipped with more flexibility since the boundaries could be moved exactly using an unstructured grid, instead of only at the discrete values corresponding to the structured grid spacing. Finally, the adaptive refinement technique could be expanded to 3D EM problems.

ACKNOWLEDGMENTS

We thank Steven Constable and Yuguo Li for useful comments, Jeff Ovall for kindly providing an advance copy of his manuscript, and Jonathan Shewchuk for making Triangle freely available. Three anonymous reviewers provided helpful suggestions for improving the manuscript. K. Key acknowledges support from the Seafloor Electromagnetic Methods Consortium at Scripps Institution of Oceanography. Sections of this work were performed at Sandia National Laboratories. Sandia is a multiprogram laboratory operated by Sandia Corporation, a Lockheed Martin Company, for the United States Department of Energy's National Nuclear Security Administration under contract DE-AC04-94AL85000.

REFERENCES

Ainsworth, M., and J. T. Oden, 2000, A posteriori error estimation in finite element analysis: John Wiley & Sons, Inc.

Aprea, C., J. Booker, and J. Smith, 1997, The forward problem of electromagnetic induction: Accurate finite-difference approximations for two-dimensional discrete boundaries with arbitrary geometry: Geophysical Journal International, **129**, 29–40.

Baba, K., and N. Seama, 2002, New technique for the incorporation of seafloor topography in electromagnetic modeling: Geophysical Journal International, **150**, 392–420.

Bank, R. E., and J. C. Xu, 2003, Asymptotically exact a posteriori error estimators, Part II: General unstructured grids: SIAM Journal on Numerical Analysis, **41**, 2313–2332.

Brewitt-Taylor, C., and J. Weaver, 1976, Finite-difference solution of 2-dimensional induction problems: Geophysical Journal of the Royal Astronomical Society, **47**, 375–396.

Coggon, J. H., 1971, Electromagnetic and electrical modeling by finite element method: Geophysics, **36**, 132–155.

Freund, R., and N. Nachtigal, 1994, An implementation of the QMR method based on coupled 2-term recurrences: SIAM Journal on Scientific Computing, **15**, 313–337.

Hohmann, G. W., 1975, Three-dimensional induced-polarization and electromagnetic modeling: Geophysics, **40**, 309–324.

Lapidus, L., and G. Pinder, 1999, Numerical solution of partial differential equations in science and engineering: Wiley Interscience.

Mackie, R. L., T. R. Madden, and P. E. Wannamaker, 1993, Three-dimensional magnetotelluric modeling using difference equations — Theory and comparisons to integral equation solutions: Geophysics, **58**, 215–226.
Mitsuhata, Y., and T. Uchida, 2004, 3D magnetotelluric modeling using the T-omega finite-element method: Geophysics, **69**, 108–119.
Newman, G. A., and D. L. Alumbaugh, 2000, Three-dimensional magnetotelluric inversion using non-linear conjugate gradients: Geophysical Journal International, **140**, 410–424.
Orange, D. L., M. M. Angell, J. R. Brand, J. Thomson, T. Buddin, M. Williams, W. Hart, and W. J. Berger III, 2004, Geologic and shallow salt tectonic setting of the Mad Dog and Atlantis fields: Relationship between salt, faults, and seafloor geomorphology: The Leading Edge, **23**, 354–365.
Ovall, J. S., 2004, Duality-based adaptive refinement for elliptic PDEs: Ph.D. thesis, University of California, San Diego.
———, 2006, Asymptotically exact functional error estimators based on superconvergent gradient recovery: Numerische Mathematik, **102**, 543–558.
Schwalenberg, K., and R. N. Edwards, 2004, The effect of seafloor topography on magnetotelluric fields: An analytic formulation confirmed with numerical results: Geophysical Journal International, **159**, 607–621.
Shewchuk, J. R., 1996, Triangle: Engineering a 2D quality mesh generator and delaunay triangulator, *in* M. C. Lin and D. Manocha, eds., Applied computational geometry: Towards geometric engineering: ACM Workshop on applied computational geometry, Springer-Verlag, 203–222.
———, 2002, Delaunay refinement algorithms for triangular mesh generation: Computational Geometry — Theory and Applications, **22**, 21–74.
Simpson, F., and K. Bahr, 2005, Practical magnetotellurics: Cambridge Univ. Press.
Siripunvaraporn, W., G. Egbert, Y. Lenbury, and M. Uyeshima, 2005, Three-dimensional magnetotelluric inversion: Data-space method: Physics of the Earth and Planetary Interiors, **150**, 3–14.
Vozoff, K., 1991, The magnetotelluric method, *in* M. N. Nabighian, ed., Electromagnetic methods in applied geophysics, vol. 2: SEG, 641–711.
Wannamaker, P., G. Hohmann, and W. San Filipo, 1984, Electromagnetic modeling of 3-dimensional bodies in layered earths using integral-equations: Geophysics, **49**, 60–74.
Wannamaker, P. E., J. A. Stodt, and L. Rijo, 1987, A stable finite-element solution for two-dimensional magnetotelluric modeling: Geophysical Journal of the Royal Astronomical Society, **88**, 277–296.
Weaver, J., B. LeQuang, and G. Fischer, 1985, A comparison of analytic and numerical results for a two-dimensional control model in electromagnetic induction, Part I, B-polarization calculations: Geophysical Journal of the Royal Astronomical Society, **82**, 263–277.
———, 1986, A comparison of analytical and numerical results for a 2-d control model in electromagnetic induction, Part II, E-polarization calculations: Geophysical Journal of the Royal Astronomical Society, **87**, 917–948.
Zhdanov, M., and E. Tartaras, 2002, Three-dimensional inversion of multitransmitter electromagnetic data based on the localized quasi-linear approximation: Geophysical Journal International, **148**, 506–519.